A statistical methodology for testing the anisotropy of Brownian textures with an application to full-field digital mammography

Frédéric Richard, Hermine Biermé

A STATISTICAL METHODOLOGY FOR TESTING THE ANISOTROPY OF BROWNIAN TEXTURES WITH AN APPLICATION TO FULL-FIELD DIGITAL MAMMOGRAPHY

FRÉDÉRIC RICHARD AND HERMINE BIERME

ABSTRACT. In this paper, we propose a new and generic methodology for the analysis of the texture anisotropy. The methodology is fundamentally based on the stochastic modeling of textures by Anisotropic Fractional Brownian Fields (AFBF). It includes some original statistical tests for deciding if a texture modeled by an AFBF is clearly anisotropic. These tests are based on the estimation of directional parameters of an AFBF by generalized quadratic variations (GQV). The construction of these tests is inspired from a new theoretical result on the convergence of the GQV estimators, which is proved in the paper. The methodology is validated and discussed on simulated data. The methodology is also applied to Full-Field Digital Mammograms (FFDM). On a database composed of 118 FFDM, we show that about 60 percent of textures can be considered as anisotropic with a high level of confidence. These empirical results strongly suggest that AFBF are better-suited than the commonly used isotropic Brownian fields for the modeling of FFDM textures.

Keywords: Anisotropy, anisotropic fractional Brownian field, Hurst index, generalized quadratic variations, texture analysis, mammography, density characterization.

1. INTRODUCTION

Texture analysis is an important generic research area of machine vision, which is being motivated by numerous applications (e.g. biomedical image analysis, analysis of satellite imagery or content-based retrieval from image databases). There is a wide variety of texture analysis approaches. Some of these approaches, such as Markov random field modeling [25] or fractal analysis [51], are based on the description of image textures with stochastic models. In such approaches, texture features are derived from the estimation of model parameters. The stochastic model beyond fractal analysis is the Fractional Brownian Field (FBF), which is a multi-dimensional extension of the famous fractional Brownian motion introduced by Mandelbrot and Van-Ness [46]. FBF is mathematically defined as the unique centered Gaussian field, null at origin, with stationary increments which is isotropic and self-similar of order $H \in (0,1)$. The variogram (see Section 2.1 for a definition) of a FBF in dimension 2 is of the form $v(x) = C_H|x|^{2H}, \forall x \in \mathbb{R}^2$. The parameter H, called the Hurst index,

Date: October 5, 2007.

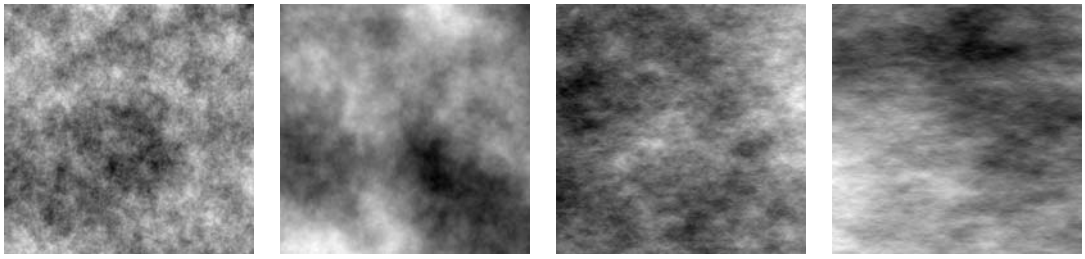

(a) (b) (c) (d)

FIGURE 1. Some field simulations. Simulation of FBF using the Stein method for (a) $h = 0.3$ and (b) $h = 0.7$. Simulation of AFBF using the spectral method for (c) $h_1 = 0.3$ and $h_2 = 0.5$ and (d) $h_1 = 0.3$ and $h_2 = 0.7$.

is a fundamental parameter of FBF which is an indicator of the texture roughness and is directly related to the fractal dimension.

The fractal analysis has been largely used in medical applications [9, 17, 21, 23, 45]. In particular, it was used for the characterization and classification of the mammogram density [21] and for the assessment of a breast cancer risk [21, 35]. The fractal analysis was also used for the radiographic characterization of the bone architecture and the evaluation of an osteoporotic fracture risk [9]. In this application, it is now well-established that the anisotropy of the bone is an important predictor of fracture risk [17, 38]. Hence the fractal analysis with FBF models, which is isotropic by definition of H, is not completely satisfactory for this application.

For defining anisotropic field models, Bonami and Estrade considered a generic class of d-dimensional Gaussian fields (with stationary increments) which are characterized by variograms of the form

$$\forall\, x \in \mathbb{R}^d, v(x) = \int_{\mathbb{R}^d} \left|e^{ix\cdot\zeta} - 1\right|^2 f(\zeta) d\zeta, \tag{1}$$

where f is a positive function such that $\int_{\mathbb{R}^d} (1 \wedge |\zeta|^2)\, f(\zeta) d\zeta < \infty$, which is called the spectral density. In dimension 2, anisotropic fields can be defined by taking spectral densities of the form

$$\forall\, \zeta \in \mathbb{R}^2, f(\zeta) = |\zeta|^{-2h(\arg(\zeta))-2}, \tag{2}$$

where h is a map taking values in $(0, 1)$ and defined for any orientation $[-\pi, \pi)$ of $\mathbb{R}^2$. Such a field will be called Anisotropic Fractional Brownian Fields (AFBF). Due to directional Hurst indices h, they have orientation-dependant spectral densities. FBF are particular AFBF characterized by a density of the form (2) with a constant function $h \equiv H$.

There are still several open issues concerning AFBF. One of them is the estimation of the directional Hurst index function h. In [5, 13], authors constructed estimators

based on generalized quadratic variations of projected fields and studied theoretically their asymptotic behavior. The asymptotic properties shown in those papers are restricted to one direction. In this paper, we present a new result which shows the convergence of linear combinations of estimators in a couple of directions. Based on this result, we build an original statistical methodology for assessing the significance of the difference between several Hurst index estimates and deciding if an observed field is anisotropic. This methodology is validated and discussed on simulated data. Finally, we apply this methodology on mammograms and study the relevance of an anisotropic model for the characterization of the textures of these images.

2. Elements of theory

2.1. **Gaussian fields with stationary increments.** Let $(\Omega, \mathcal{A}, \mathbb{P})$ be a probability space. A d-dimensional random field X is a map from $\Omega \times \mathbb{R}^d$ into $\mathbb{R}$ such that $X(\cdot, y) := X(y)$ is a real random variable on Ω for all $y \in \mathbb{R}^d$. When $d = 1$, such a field is called a random process. We say that a random field is Gaussian if any finite linear combination of its associated random variables is a Gaussian variable. A centered Gaussian field X is characterized by its covariance function: $(y, z) \mapsto \mathrm{Cov}(X(y), X(z))$. A field X has stationary increments if the law governing the field $X(\cdot + z) - X(z)$ is the same as $X(\cdot) - X(0)$ for all $z \in \mathbb{R}^d$. A centered Gaussian field X with stationary increments is characterized by its variogram, which is defined by

$$\forall y \in \mathbb{R}^d, \;\; v(y) = \mathbb{E}((X(y) - X(0))^2). \tag{3}$$

In what follows, we will consider centered Gaussian fields with stationary increments, which have a variogram of the form (1). Such fields are referred to as Gaussian Fields with Spectral Density (GFSD).

2.2. **Review of some FBF extensions.** Due to its extensive use in fractal analysis, FBF is the most famous GFSD. The isotropy of FBF is a serious limitation for the modeling of fields showing different behaviors in several directions. Hence, several extensions of FBF have been proposed to obtain anisotropic models. In [28], FBF model was generalized by considering fields with variograms of the form

$$\forall y \in \mathbb{R}^d, \;\; v(y) = C\left(\frac{y}{|y|}\right)|y|^{2H},$$

where C is a function called the "topothesy function" which is orientation-dependant. Some of these fields are GFSD with spectral density given by

$$\forall \zeta \in \mathbb{R}^d, \;\; f(\zeta) = c\left(\frac{\zeta}{|\zeta|}\right)|\zeta|^{-2H-d}.$$

In this model, the Hurst exponent H does not depend on the direction. In [39], Kamont introduced the so-called fractional Brownian sheet. This model has different Hurst indices in an orthogonal basis of directions. In [44], the Brownian sheet was constructed by fractional integration with respect to a white noise and used for

the modeling of bone radiographs and the characterization of the osteoporosis. In [10, 12], the so-called operator scaling Gaussian random fields were introduced for the modeling of sedimentary aquifers. As for the Brownian sheet, Hurst indices of these fields are different on some directions, but those directions are not necessarily orthogonal. Contrarily to fractional Brownian sheets, these fields have stationary increments. They are GFSD with spectral density satisfying

$$\forall \zeta \in \mathbb{R}^d\,,\ \ f(c^E\zeta) = c^{-2H-\mathrm{tr}(E)} f(\zeta),$$

for a real $d\times d$-matrix E and $H>0$. Such fields generalize FBF, which are obtained with $E=I_d$ (the identity matrix). Let us also mention that sample path properties of these three kinds of anisotropic random fields, such as modulus of continuity, local times and Hausdorff dimensions, were studied in [57].

The multi-fractional Brownian motion defined simultaneously in [8] and [50] is another generalization of FBF. In this model, the Hurst index H of FBF is replaced by a function depending on the point $y \in \mathbb{R}^d$. Such models are not necessarily anisotropic and have non-stationary increments.

In this paper, we will focus on AFBF as introduced in [14] in dimension $d=2$. They are GFSD with spectral density of the form (2) in dimension 2. In dimension d, the spectral density of a AFBF is more generally defined as

$$\forall \zeta \in \mathbb{R}^d\,,\ \ f(\zeta) = |\zeta|^{-2h(\zeta/|\zeta|)-d}.$$

The function $h : S^{d-1} \to (0,1)$ characterizes the anisotropy and is called directional Hurst index.

2.3. **Field Hölder regularity.** The random field regularity is usually defined using Hölder exponents. For $T>0$, sample paths of X satisfy a uniform Hölder condition of order $\alpha \in (0,1)$ on $[-T,T]^d$ if there exists a positive random variable A with $\mathbb{P}(A<+\infty)=1$ such that

$$\forall y,z \in [-T,T]^d,\ \ |X(y)-X(z)| \le A|y-z|^\alpha. \tag{4}$$

This equation gives a lower bound for the Hölder regularity of a field. The critical Hölder exponent β of a field is defined as the supremum of α for which the Hölder condition (4) holds. From an image point of view, the critical Hölder exponent is related to the roughness of the texture. The texture is as rough as the field regularity β is small. As stated in the next theorem proved in [14], the Hölder regularity of a GFSD can either be deduced from the local behavior of the variogram around 0 (condition (iii)) or from the asymptotic behavior of the spectral density at high-frequencies (conditions (i) and (ii)).

Theorem 2.1. *Let X be a GFSD and $\beta \in (0,1)$.*
(a) If, for any $0<\alpha\le H\le\gamma<1$, there exist $A, B_1, B_2 > 0$ and a positive-measure subset E of the unit sphere S^{d-1} of $\mathbb{R}^d$ such that for almost all $\xi \in \mathbb{R}^d$,
(i): $|\xi| \ge A \Rightarrow |f(\xi)| \le B_1|\xi|^{-2\alpha-d}$,
(ii): $|\xi| \ge A$ and $\frac{\xi}{|\xi|} \in E \Rightarrow |f(\xi)| \ge B_2|\xi|^{-2\gamma-d}$.

Then, there exists $\delta > 0$ and $C_1, C_2 > 0$ such that
(iii): $\forall |y| \leq \delta, C_1|y|^{2\gamma} \leq v(y) \leq C_2|y|^{2\alpha}$.
(b) Condition (iii) implies that X admits H as critical Hölder exponent.

2.4. **Process Hölder regularity.** For random processes ($d = 1$), we will use an extended definition of the Hölder regularity which has a meaning when $\beta \geq 1$ [14]. Let $Y = \{Y(t); t \in \mathbb{R}\}$ be a centered Gaussian random process with stationary increments and variogram v. Let $t \in \mathbb{R}$. If the sequence $\left(\frac{Y(t+h)-Y(t)}{h}\right)$ admits a limit in $L^2(\Omega, \mathcal{A}, \mathbb{P})$ as $h \to 0$, we say that Y is mean-square differentiable at point t. We denote by $Y'(t)$ the corresponding limit, which is a centered Gaussian variable (see for instance page 27 of [3]). When this holds for any $t \in \mathbb{R}^d$, the variogram v of Y is two times differentiable, the process Y' is stationary and its variogram satisfies

$$(5)\ v_{Y'}(t) = -\left(v''(t) - v''(0)\right) \ = \ \lim_{h \to 0} h^{-2}\mathbb{E}\left(Y(t+h) - Y(t) - Y(h) + Y(0)\right)^2.$$

Recursively, we can further define the n-time mean square differentiable of a process Y as the mean square derivative of the $Y^{(n-1)}$ (if it exists). We then define the extended Hölder regularity. Let $\beta = n+s$, with $n \in \mathbb{N}$ and $s \in (0,1)$. We say that Y admits β as critical Hölder exponent, if Y is (a) n-time mean square differentiable and (b) its n^{th} mean square derivative admits $s = \beta - n \in (0,1)$ as critical Hölder exponent. As stated in the following theorem, the extended Hölder regularity of a process can also be deduced from the behavior of its variogram behavior around 0 and asymptotic properties of the spectral density.

Theorem 2.2. *Let $Y = \{Y(t); t \in \mathbb{R}\}$ be a Gaussian random process with spectral density. Let $\beta = n + s$, with $n \in \mathbb{N}$ and $s \in (0,1)$.*
(a) If, for any $0 < \alpha \leq s \leq \gamma < 1$, there exist $A, B_1, B_2 > 0$ such that for almost all $\xi \in \mathbb{R}$,
(i) $|\xi| \geq A \Rightarrow B_1|\xi|^{-2\gamma-2n-1} \leq f_Y(\xi) \leq B_2|\xi|^{-2\alpha-2n-1}$. Then,
(ii) the variogram v_Y is of class $\mathcal{C}^{2n}$ in a neighborhood of 0
(iii) there exists $\delta > 0$ and $C_1, C_2 > 0$ such that
$\forall |t| \leq \delta$, $C_1|t|^{2\gamma} \leq \left|v^{(2n)}(t) - v^{(2n)}(0)\right| \leq C_2|t|^{2\alpha}$.
(b) Conditions (ii) and (iii) imply that the process Y admits β as critical Hölder exponent.

2.5. **Regularity of an AFBF.** A direct application of Theorem 2.1 shows that the critical Hölder exponent of an AFBF (in dimension $d = 2$) is equal to the minimal value H of the Hurst index function h on $[-\pi, \pi)$:

$$(6) \qquad H = \operatorname{essinf}_{[-\pi,\pi)}(h).$$

The critical Hölder exponent H of an AFBF will be called the minimal Hurst index. In the particular FBF case, the minimal Hurst index is the usual Hurst index. The minimal Hurst index can be considered as a fundamental parameter which characterizes the AFBF texture roughness by giving the Hölder regularity. Note

also that the minimal Hurst index of an AFBF is related to the Hausdorff and Box-counting fractal dimensions of its graph $\mathcal{G}(X) = \{(y, X(y)) \; ; \; y \in [-T, T]^2\}$

$$\dim_{\mathcal{H}}\mathcal{G}(X) = \; \dim_{\mathcal{B}}\mathcal{G}(X) = 2 + 1 - H = 3 - H, \tag{7}$$

almost surely, for any $T > 0$ (refer to [31] for the dimension definitions). The minimal Hurst index, being direction-independent, does not capture any anisotropic feature of an AFBF.

2.6. **Regularity on oriented lines.** In attempt to characterize the anisotropy of an AFBF, one could propose to study the field along oriented straight lines. Then, the question arises to know whether or not the Hölder regularity of an AFBF along a line is somehow related to the Hurst index in the direction of the line.
In the general setting of dimension d, let us parametrize any line Δ of $\mathbb{R}^d$ with $(t_0, \theta) \in \mathbb{R}^d \times S^{d-1}$ and define $X_\Delta = \{X(t_0 + t\theta); t \in \mathbb{R}\}$ the restriction of a field X on the line Δ. If X is a GFSD, any restriction X_Δ is a Gaussian process with spectral density given by

$$\forall p \in \mathbb{R}, \; f_\Delta(p) = \int_{\langle\theta\rangle^\perp} f(\xi + p\theta) d\xi, \tag{8}$$

where f is the spectral density of X and $\langle\theta\rangle^\perp$ denotes the hyperplane of $\mathbb{R}^d$ orthogonal to the direction θ. When X is an AFBF and $d = 2$, it can be shown that for any line Δ, conditions (i) and (ii) of the Theorem 2.1 hold for the spectral density of X_Δ with $H = \text{essinf}_{[-\pi,\pi]}(h)$. In other words, for any chosen line Δ, the critical Hölder exponent of X_Δ is constant and equal to the minimal Hurst index. Therefore, it is not possible to study directional Hurst indices of an AFBF using line-restrictions.

2.7. **Projection regularity.** As an alternative to line-restrictions, Bonami and Estrade proposed to study windowed Radon transforms of fields [14]. These transforms are defined in the general setting of dimension d, by projecting a field X along hyperplanes $\langle\theta\rangle^\perp$ of $\mathbb{R}^d$:

$$\forall (\theta, t) \in S^{d-1} \times \mathbb{R}, \;\; R_\rho X(\theta, t) = \int_{\langle\theta\rangle^\perp} X(s + t\theta)\rho(s) ds, \tag{9}$$

where ρ is a window function of the Schwartz class such that $\int_{\mathbb{R}} \rho(\gamma) d\gamma = 1$. Then, the question arises to know if the regularity of the process $R_\rho X(\theta, t)$ is related to the Hurst index of X in the direction θ. For any direction $\theta \in S^{d-1}$, the obtained process $R_\theta X = \{R_\rho X(\theta, t), t \in \mathbb{R}\}$ is a Gaussian process with a spectral density given by

$$\forall p \in \mathbb{R}, \;\; \mathcal{R}_\theta f(p) = \int_{\langle\theta\rangle^\perp} f(\xi + p\theta) \left|\widehat{\rho}(\xi)\right|^2 d\xi, \tag{10}$$

where f is the spectral density of X. For an AFBF, it was shown that the spectral density of $R_\theta X$ checks condition (i) of Theorem 2.2 for $\beta(\theta) = h(\theta) + 1/2$. In other words, the Hölder regularity of the projected field $R_\theta X$ is equal to $h(\theta) + 1/2$ and depends on the direction θ along which the projection is performed. The parameter

$\frac{1}{2}$ corresponds to the smoothing effect of the projection which is equal to $\frac{d-1}{2}$ ($d = 2$). By estimating the regularity of the process $R_\theta X$, it is thus possible to estimate the value $h(\theta)$ and study the anisotropy of an AFBF.

3. Estimation Method

As mentioned above, the directional Hurst index $h(\theta)$ of an AFBF can be deduced from the critical Hölder exponent of the projected field $R_\rho X(\theta, \cdot)$ along the direction θ. Since this projected field is a one-dimensional fractional Brownian motion (fBm), it is possible to use estimation techniques which have been developed for such processes. Up to now, many estimators of the Hurst index of a fBm have been proposed (see [24] and [7] and references therein for a review). The maximum likelihood estimator, the related Whittle estimator [11], and the wavelet-based estimators [1] are often used for analyzing fBm with long-range dependence ($H \in (1/2, 1)$). These estimators are consistent and have an asymptotic normality. Some other estimators are defined by a filtering of discrete observations of a fBm sample path. This is the case with Generalized Quadratic Variations (GQV) studied in [37, 42]. Such estimators are particularly interesting: (i) they can be used for the estimation of the regularity of a large class of Gaussian fields which includes fBm, (ii) they are also consistent and have asymptotic normality. Due to the good properties of GQV, we chose the GQV for the estimation of directional Hurst indices in this study.

3.1. Generalized Quadratic Variations.

Let Y_θ be the projected field $R_\rho X(\theta, \cdot)$ of an AFBF X, as defined by Equation (9). Let $M = 2^m$, for an integer $m \geq 1$. For any $\nu \in \mathbb{N}$, $\nu < m$, $u \in \mathbb{N}\backslash\{0\}$, we define second-order increments $Z^\nu_{\theta,u}$ of Y_θ

$$Z^\nu_{\theta,u}(t) = Y_\theta\left(\frac{t+2u}{2^{-\nu}M}\right) - 2Y_\theta\left(\frac{t+u}{2^{-\nu}M}\right) + Y_\theta\left(\frac{t}{2^{-\nu}M}\right). \tag{11}$$

The value $1/2^{-\nu}M$ can be seen as a precision at which Y_θ is considered and $u/2^{-\nu}M$ as an increment step. Due to assumptions on Y_θ, the process $Z^\nu_{\theta,u}$ is stationary. The generalized quadratic variations of Y_θ of order 2 are defined as

$$V^\nu_{\theta,u} = \frac{1}{2^{-\nu}M - 2u + 1} \sum_{p=0}^{2^{-\nu}M-2u} (Z^\nu_{\theta,u}(p))^2. \tag{12}$$

By ergodicity, one can prove that $V^\nu_{\theta,u} \underset{2^{-\nu}M\to+\infty}{\sim} \mathbb{E}(V^\nu_{\theta,u})$. Moreover,

$$\mathbb{E}(V^\nu_{\theta,u}) = \mathbb{E}((Z^\nu_{\theta,u}(0))^2) = \mathbb{E}\left(Y_\theta\left(\frac{2^\nu u}{M} + \frac{2^\nu u}{M}\right) - 2Y_\theta\left(\frac{2^\nu u}{M}\right) + Y_\theta(0)\right)^2,$$

Comparing this equation to Equation (5), we can interpret $\mathbb{E}(V^\nu_{\theta,u})$ as a second order discrete derivative of the variogram around 0. Due to application of Theorem 2.2 to Y_θ, the critical Hölder exponent of $Z^\nu_{\theta,u}$ is $h(\theta) + 1/2$ and the asymptotic behavior

of the variogram of $Z^\nu_{\theta,u}$ is known (condition (ii)). As a result, one can show that

$$\mathbb{E}(V^\nu_{\theta,u}) \underset{2^{-\nu}M\to+\infty}{\sim} C(2^{-\nu}M)^{-2h(\theta)-1}u^{2h(\theta)+1}. \tag{13}$$

From this asymptotic property of GQV, we can heuristically derive an estimator of $h(\theta)$ based on GQV of Y_θ, namely

$$\hat{H}^\nu(\theta) = \frac{1}{2\log(2)}\log\left(\frac{V^\nu_{\theta,2}}{V^\nu_{\theta,1}}\right) - \frac{1}{2}. \tag{14}$$

The proof and theoretical conditions for this estimator to converge to $h(\theta)$ as $2^{-\nu}M$ tends to $+\infty$ can be found in [13].

3.2. **Anisotropy test.** Let us consider the case of an AFBM X with spectral density f satisfying

$$f(\xi) = \begin{cases} |\xi|^{-(2h_1+2)}, & \text{if } |\xi_1| < c_1|\xi_2| \\ |\xi|^{-(2h_2+2)}, & \text{if } |\xi_2| < c_2|\xi_1|, \end{cases} \tag{15}$$

with $0 < c_2 < c_1^{-1}$. Let us denote $\hat{H}^\nu_1 = \hat{H}^\nu(0,1)$ and $\hat{H}^\nu_2 = \hat{H}^\nu(1,0)$ the estimators of the directional Hurst exponent in vertical and horizontal directions.

Theorem 3.1. *Let X be an AFBM with spectral density f satisfying* (15)*. Then, almost surely*

$$\hat{H}^\nu_1 - \hat{H}^\nu_2 \underset{2^{-\nu}M\to+\infty}{\longrightarrow} h_1 - h_2$$

with, for some $\gamma > 0$,

$$\sqrt{2^{-\nu}M}\left(\hat{H}^\nu_1 - \hat{H}^\nu_2 - (h_1 - h_2)\right) \underset{2^{-\nu}M\to+\infty}{\xrightarrow{d}} \mathcal{N}\left(0,\gamma^2\right).$$

This theorem is proved in appendix A. It is the theoretical contribution of the paper to the study of estimator asymptotics for AFBF models.

In addition to its theoretical interest, Theorem 3.1 can be used heuristically for testing the isotropy of an AFBF. Let us consider the statistical asymptotic hypothesis test for testing the assumption $\mathbf{H}_0$: $h_1 = h_2$ (isotropy) against $\mathbf{H}_1$: $h_1 \neq h_2$ (anisotropy). Our test statistic is naturally defined by

$$D^\nu_M = \sqrt{2^{-\nu}M}\left|\hat{H}^\nu_1 - \hat{H}^\nu_2\right|. \tag{16}$$

By Theorem 3.1, under the assumption $\mathbf{H}_0$ we have $D^\nu_M \underset{2^{-\nu}M\to+\infty}{\xrightarrow{d}} |\mathcal{N}(0,\gamma^2)|$ while $D^\nu_M \underset{2^{-\nu}M\to+\infty}{\longrightarrow} +\infty$ under the assumption $\mathbf{H}_1$. Hence, we define the form of an hypothesis rejection interval (of confidence level α) as

$$\mathcal{R}^\nu = \{D^\nu_M > \gamma\, t_\alpha\}, \tag{17}$$

where t_α stands for $(1-\alpha/2)$-quantile of the centered and normalized Gaussian distribution.

3.3. **Implementation.** Assume we observe a 2-dimensional realization of a field x on the uniform grid $\{\left(\frac{k}{M},\frac{l}{M}\right), 0 \leq k,l \leq M\}$ of $[0,1]^2$ at resolution $1/M$. We denote by $x(k,l)$ the value of the observed field at position $\left(\frac{k}{M},\frac{l}{M}\right)$. We first compute discrete row- and column-wise averages (y_1 and y_2) of x:

$$\forall\, 0 \leq k,l \leq M,\ \ y_1(l) = \frac{1}{M}\sum_{k=0}^{M} x(k,l) \ \text{ and } \ y_2(k) = \frac{l}{M}\sum_{l=0}^{M} x(k,l). \tag{18}$$

We then compute discrete quadratic variations $v^\nu_{e,u}$ in both directions ($e = 1,2$) for dilation parameters $u = 1,2$ and different values of ν (such that $2^{\nu+1}u < M$)

$$v^\nu_{e,u} = \frac{1}{\tilde{M}+1}\sum_{p=0}^{\tilde{M}} (y_e(sp) - 2\, y_e(s(p+u)) + y_e(s(p+2u)))^2, \tag{19}$$

with $s = 2^\nu$ and $\tilde{M} = M/2^\nu - 2u$. Finally, we define the discrete projection-based estimator $\hat{h}^\nu_e$ of the index h_e of X in directions $e = 1,2$

$$\hat{h}^\nu_e = \frac{1}{2\log(2)}\log\left(\frac{v^\nu_{e,2}}{v^\nu_{e,1}}\right) - \frac{1}{2}. \tag{20}$$

The effect of discretizations on the estimation is one of the main theoretical issue which was investigated in [13]. We have shown that the estimation error due to the approximation of $V^\nu_{\theta,u}$ by $v^\nu_{e,u}$ is controlled by the inequality

$$\left|\log(v^\nu_{e,u}/V^\nu_{\theta,u})\right| \leq C'' M^{-\alpha}(M/2^\nu)^{h(\theta)+1/2},$$

for any $\alpha < H$, where H is the minimal Hurst index. We then established the convergence of $\hat{h}^\nu_e$ to $h(\theta)$ as $M = 2^m$ tends to $+\infty$ under condition that $\nu > m\frac{h(\theta)-H+1/2}{h(\theta)+1/2}$. This condition is purely theoretical and cannot be used in practice. We rely on a numerical study to fix an optimal value of ν (see Section 5).

For the estimation of the minimal Hurst index H (see Equation (6)), we also use a line-based estimator. We define discrete line-restrictions z^h_e of x in the row and column direction $e = 1,2$.

$$\forall\, 0 \leq k,l \leq M,\ \ z^k_1(l) = x(k,l) \ \text{ and } \ z^l_2(k) = x(k,l). \tag{21}$$

We then compute the discrete quadratic variations w^j_e of these restrictions

$$w^j_{e,u} = \frac{1}{M-2u}\sum_{p=0}^{M-2u} (z^j_e(p) - 2\, z^j_e(p+u) + z^j_e(p+2u))^2, \tag{22}$$

for $u = 1, 2$ and $0 \leq j \leq M$. Next, we compute estimates $\hat{h}_{0e}$ of Hurst indices in row and column directions $e = 1, 2$ as

$$\hat{h}_{0e} = \frac{1}{2\log(2)} \log \left(\frac{\sum_{j=0}^{M} w_{e,2}^{j}}{\sum_{j=0}^{M} w_{e,1}^{j}} \right), \tag{23}$$

We finally consider the estimate of the minimal Hurst index given by

$$\hat{H} = \min(\hat{h}_{01}, \hat{h}_{02}). \tag{24}$$

The convergence of these line-based estimators to the minimal Hurst index as M tends to $+\infty$ can be established using theorems shown in [13].

Besides, using the discrete projection-based estimators in both directions, we can define an empirical statistical test for testing the assumption $\mathbf{H}_0$: $h_1 = h_2$ (isotropy) against $\mathbf{H}_1$: $h_1 \neq h_2$ (anisotropy). Let $\hat{d}^{\nu} = |\hat{h}_1^{\nu} - \hat{h}_2^{\nu}|$ be the empirical approximation of the statistic $\frac{D_M^{\nu}}{\sqrt{2^{-\nu}M}}$ in Equation (16), with $\hat{h}_1^{\nu}$ and $\hat{h}_2^{\nu}$ given by (20). The rejection interval of confidence level $\alpha = 0.05$ for the above test is defined as

$$R^{\nu} = \{\hat{d}^{\nu} > 1.96\sigma\}, \tag{25}$$

where 1.96 is the 0.975-quantile of the centered and normalized Gaussian distribution and $\sigma = \frac{\gamma}{\sqrt{2^{-\nu}M}}$ is the standard deviation of $\hat{d}^{\nu}$. This empirical test will be referred to as the first anisotropy test. Theorem 3.1 does not however give an explicit value of γ, nor the optimal choice for ν. These two parameters will be set empirically in Section 5.

This test evaluates the anisotropy between vertical and horizontal directions. Hence it cannot detect anisotropic fields which have the same vertical and horizontal directional Hurst indices. In order to fix this drawback, we set a second anisotropy test which takes into account the other directions using an estimation of the minimal directional Hurst index H: we test the assumption $\mathbf{H}_0$: $H = h_1 = h_2$ (isotropy) against $\mathbf{H}_1$: $H \neq h_1$ or $H \neq h_2$ (anisotropy). We consider the empirical statistic $\hat{\delta}^{\nu} = |\max(\hat{h}_1^{\nu}, \hat{h}_2^{\nu}) - \hat{H}|$, with $\hat{h}_1^{\nu}$, $\hat{h}_2^{\nu}$ given by (20) and $\hat{H}$ by (24). The rejection interval of the test is then defined by

$$R^{\nu} = \{\hat{\delta}^{\nu} > c\}, \tag{26}$$

where c is a positive constant which will be fixed empirically in Section 5.

4. Field synthesis

A lot of numerical methods have been recently proposed to simulate 1-dimensional fractional Brownian motion (fBm) [6]. Most of them are approximation methods. This is the case of the midpoint displacement method [48] and the wavelet based decomposition [2, 47, 53]. A few of them can be generalized to the simulation of 2-dimensional (anisotropic) fractional Brownian fields. Methods based on the

Choleski decomposition of the covariance function generate exact synthesis but also cause numerical problems due to the size of the matrix. In order to have a fast synthesis one can use the stationarity of the increments by applying the embedding circulant matrix method [29]. By this way, we easily obtain fast and exact synthesis of 1-dimensional fBm [52]. Some authors apply this method for higher dimension but this does not produce exact synthesis in general [22, 40].

4.1. **The Stein method.** The embedding circulant matrix method is a famous and efficient algorithm for the synthesis of a stationary Gaussian random field. It is based on the fact that the covariance matrix of a stationary field is Toeplitz. It consists of embedding this matrix in a larger symmetric matrix which is circulant and thus diagonalizable by discrete Fourier transform. This yields to a fast and exact algorithm as soon as the eigenvalues of the embedding circulant matrix are positive. This method is well-suited for the generation of increments of a fractional Brownian motion (dimension 1). However it cannot be applied in dimension 2 because the eigenvalues of the minimal embedding circulant matrix of FBF increments are not positive. To fix this problem, Stein proposed a method which consists of two steps: (1) The generation of an isotropic stationary Gaussian random field which have a minimal positive embedding circulant covariance matrix and is "close" to a FBF increment, (2) the transformation of this initial field into an exact simulation of a FBF [54].

Let B_H be a FBF with Hurst index $H \in (0,1)$ and recall that

$$\mathrm{Var}\left(B_H(x) - B_H(y)\right) = |x-y|^{2H}, \forall\, x, y \in \mathbb{R}^2.$$

Let us define a covariance K as:

$$K(x-y) = \begin{cases} c_0 - |x-y|^{2H} + c_2|x-y|^2 & \text{if } 0 \leq |x-y| \leq 1 \\ 0 & \text{otherwise} \end{cases},$$

with constants $c_0 = 1 - H$ and $c_2 = H$. The additional term $c_2|x-y|^2$ ensures the positiveness of the minimal embedding circulant matrix of K. We can thus simulate a random field Z with covariance K. Whenever $|x-y| \leq 1$, we have

$$\mathrm{Var}(Z(x) - Z(y)) = \mathrm{Var}(B_H(x) - B_H(y)) - 2c_2|x-y|^2.$$

Independently of Z, we generate two independent random variables X_1 and X_2 with the same Gaussian law $\mathcal{N}(0, 2c_2)$. We define the random field

$$Z^*(x) = Z(x) + x_1 X_1 + x_2 X_2 - Z(0),$$

with $x = (x_1, x_2) \in \mathbb{R}^2$. When $|x| \leq 1$, $|y| \leq 1$ and $|x-y| \leq 1$,

$$\mathbb{E}(Z^*(x)Z^*(y)) = \mathbb{E}(B_H(x)B_H(y)).$$

Therefore, the random field $Z^* = \{Z^*(x); |x| \leq 1\}$ is a standard FBF of Hurst parameter H. Stein proved that this choice of K leads to an exact simulation when $H \in (0, 0.75)$. Some simulation examples are shown on Figures 1 (a) and (b). Let us point out that the main difficulty of this method is to prove that K is well-defined as a covariance function. For this reason, the method can not be easily generalized.

4.2. **The spectral method.** The Stein method cannot be generalized to simulate anisotropic fields. We thus propose another simulation method based on a discretization of the spectral representation of an AFBF [14]. The directional Hurst indices of 2-dimensional AFBF we generate differs in both row and column directions. The spectral densities of these fields are of the form

$$f(\xi) = \begin{cases} |\xi|^{-(2h_1+2)}, & \text{if } |\xi_1| < |\xi_2| \\ |\xi|^{-(2h_2+2)}, & \text{otherwise.} \end{cases} \tag{27}$$

for all $\xi = (\xi_1, \xi_2) \in \mathbb{R}^2 \setminus \{(0,0)\}$. In this expression, h_1 and h_2 form a pair of parameters in $(0,1)$ which characterize the anisotropy of generated fields. The minimal Hurst index of the generated field is $H = \min(h_1, h_2)$ (see Section 2.5).

Define $g(x,y) = f^{1/2}(x,y)$ for all $(x,y) \in [-M,M]^2 \setminus \{(0,0)\}$ and $g(0,0) = 0$. Let $\{z(n_1,n_2), 0 \leq n_1, n_2 \leq M\}$ be $(2M+1)^2$ independent realizations of complex random variables whose real and imaginary components are two uncorrelated zero-mean standard Gaussian variables.We generate a random field y using a discrete spectral representation. For $0 \leq n_1, n_2 \leq M$, values $y(\frac{k_1}{M}, \frac{k_2}{M})$ are given by

$$\pi \sum_{n_1,n_2=-M+1}^{M} z(n_1,n_2)\, g(\pi n_1, \pi n_2) e^{-\frac{i\pi}{M}(n_1k_1+n_2k_2)}. \tag{28}$$

We then define an approximated AFBF as $x(\frac{k_1}{M}, \frac{k_2}{M}) = \Re(y(\frac{k_1}{M}, \frac{k_2}{M}) - y(0,0))$, for $0 \leq k_1, k_2 \leq M$. From a practical view point, the sum in previous Equation is a filtering in the Fourier domain of a white noise z by a low-pass linear filter with transfer function g. Based on this method, AFBF approximations can be easily and quickly simulated using a fast Fourier transform. Some simulation examples are shown on Figures 1 (c) and (d).

5. Numerical Study

We used the simulation methods presented in Section 4 for generating a dataset of synthetic textures. This dataset has two parts. The first part contains 8 subsets of 1000 FBF of size 512×512 generated using Stein method eight different Hurst index values. The second part contains six subsets of 1000 fields of size 512×512 simulated using the spectral method with various pairs of parameter values (h_1, h_2). We applied projection-based estimators $\hat{h}_e^\nu$ (Equation (20)) with different sampling factors ν for the estimation of Hurst indices of each simulated field in two directions ($e = 1$: row direction, $e = 2$: column direction).

5.1. **Estimator precision.** We evaluated the accuracy and the precision of each estimator on the different sets. The accuracy of an estimator on a given set was obtained by averaging parameter estimates over the set and subtracting the true parameter value; it is the empirical bias of the estimator. The precision of an estimator on a given set was defined as the standard deviation of parameter estimates over the set. Accuracy and precision are both reported in Figures 2.

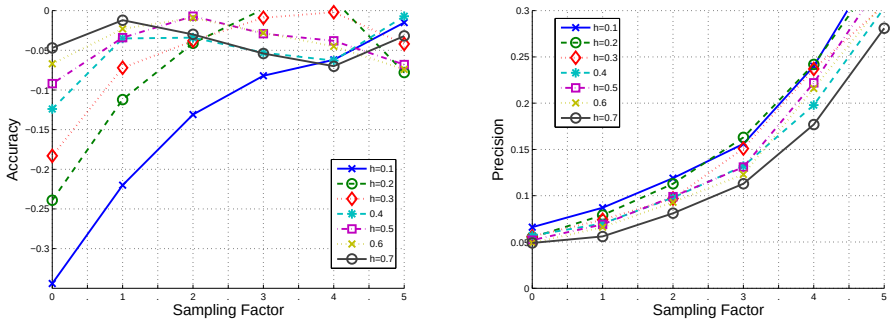

FIGURE 2. Projection-based estimation of global Hurst index on isotropic fields simulated using the Stein method. The accuracy and precision of the projection-based estimators $\hat{h}_e^{\nu}$ $(e = 1, 2)$ are computed for different global Hurst index values of fields and different estimator sampling factors.

(a) Sampling factor $\nu = 0$. (b) Sampling factor $\nu = 1$.

(c) Sampling factor $\nu = 2$. (d) Sampling factor $\nu = 3$.

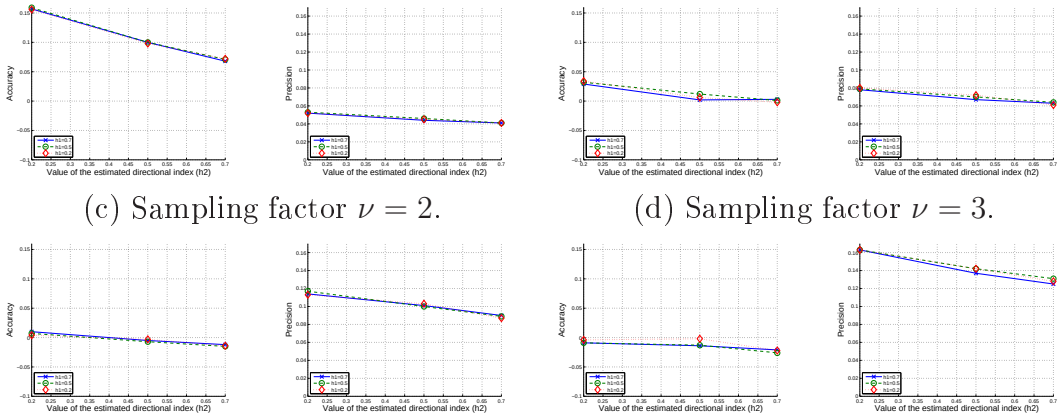

FIGURE 3. Projection-based estimation of the directional Hurst index h_2 on fields simulated using the spectral method. The accuracy and precision of vertical projection-based estimators $\hat{h}_2^{\nu}$ are computed for different couples of vertical and horizontal Hurst index values of simulated fields and different sampling factors.

Figure 2 shows that accuracy and precision both depends on the estimator sampling factor. The precision becomes worse and worse as the sampling factor increases: when the sampling factor is increased, the size of the increment process becomes smaller, reducing the number of points used for the variation-based estimation and the reliability of the estimator. However, when the sub-sampling factor

is fixed, the precision does not vary significantly when values of the estimated index are changed. For any fixed sampling factor below 4, the precision variations are of order 0.05. For comparison, the precision of the line-based estimator of the Hurst index is about 0.02 for any index value and its bias is 0. Hence, even when $\nu = 0$, projection-based estimators are less reliable for the estimation of the Hurst index than line-based estimators. This is an effect of the projection on the estimation. Concerning the accuracy, estimators tend to underestimate the real index value. The underestimation bias increases as the index value decreases. For any estimated index value h, the accuracy further varies as a function of the sampling factor and reaches an optimum for a sampling factor value $\nu_{\text{opt}}(h)$. The accuracy optima are almost the same for the different index values. However, the optimal sampling values $\nu_{\text{opt}}(h)$ are different: it is higher for low index values than for high index values. Considering index values altogether, the best accuracy seems to be reached for $\nu = 2$. In this case, the estimation error is below 0.05 for all index values varying between 0.2 and 0.8 and around 0.13 for the index value 0.1. The precision achieved for the same sampling factor $\nu = 2$ is about 0.1. The sampling factor $\nu = 2$ gives a good compromise between accuracy and precision and will be used to measure directional indices in applications.

On Figure 3, we notice that the accuracy results obtained for isotropic fields ($h_1 = h_2$) simulated with the spectral method are not consistent with the previous discussion on Figure 2. Indeed, curves on Figure 3 shows that estimators overestimate index values. This difference between both results is probably due to the simulation methods. The spectral simulation method is likely to generate fields which are smoother than what they should be whereas the Stein method is exact. However, we can rely on results of Figure 3 to get a sense of the estimator properties when fields are anisotropic. When the sampling factor is fixed, precisions are about the same for isotropic and anisotropic simulations. Accuracies still vary when estimated parameter values are changed. However, the accuracy of the Hurst index estimator $\hat{h}_1$ does not depend on the index value h_2 in the other direction.

5.2. **Anisotropy test.** We evaluated the accuracy and precision of the estimation of the Hurst index difference $d = |h_1 - h_2|$ by the estimators $\hat{d}^\nu = |\hat{h}_1^\nu - \hat{h}_2^\nu|$, for $\nu = 0, 2$. Results are reported in Tables 1 and 2. As expected the accuracy depends on the pair of Hurst indices which is estimated. The precision is however quite stable: it is around 0.08 when $\nu = 0$ and 0.15 when $\nu = 2$ (Table 1). We used these precision values as estimates of the standard deviation γ of the test statistic $\hat{d}^\nu$ (see Section 3.2). This enables to set two rejection intervals for the anisotropy test described in Section 3.3: one interval for $\nu = 0$ which is $R^0 = \{|\hat{d}^0| > 0.16\}$ and another for $\nu = 2$ which is $R^2 = \{|\hat{d}^2| > 0.3\}$. We applied these tests to Stein and spectral simulations and reported results in Tables 1 and 2. On isotropic simulations, tests produce few errors, whatever the value of the minimal Hurst index, but results are slightly better when the Hurst index is high. Results of tests with $\nu = 0$ and $\nu = 2$ are not significantly different on isotropic fields. On anisotropic fields, the test for $\nu = 0$ is

	$\nu=0$		$\nu=2$	
h	$\hat{d}^0 \pm \sigma$	p	$\hat{d}^2 \pm \sigma$	p
0.1	-0.02±0.1	89	0.±0.17	91
0.2	0.±0.08	95	0.01±0.16	94
0.3	-0.01±0.09	93	0.±0.16	94
0.4	0.±0.08	96	0.±0.16	94
0.5	0.±0.08	97	0.01±0.14	98
0.6	0.±0.07	98	0.01±0.14	97
0.7	0.±0.06	99	0.±0.13	99
T	0.±0.08	95	0.±0.15	95

TABLE 1. Estimation of the directional Hurst index differences $h_1 - h_2$ on FBF simulated with Stein simulation technique. The value p is the percentage of simulations classified into isotropic using the anisotropy test on statistics $\hat{d}^\nu$.

however more powerful than for $\nu = 2$. When $\nu = 2$, the test does not detect the anisotropy when Hurst index differences $|h_1 - h_2|$ are below 0.2 (between 74 and 84 % of detection errors). However, the efficiency of the test is improved as differences increase. Similarly, when $\nu = 0$, the test is not efficient when Hurst index differences are below 0.2 (between 32 and 43 % of errors). However, it becomes reliable when differences are above 0.3 (0 % of errors). As mentioned previously, the statistic $\hat{d}^0$ used in the test with $\nu = 0$ is more biased than the one with $\nu = 2$. However, the test with $\nu = 0$ has better results than with $\nu = 2$ because the statistic $\hat{d}^0$ is more precised than $\hat{d}^2$.

In Tables 3 and 4, we present the mean values and standard deviations of the statistic $\hat{\delta}^\nu$ used in the second anisotropy test (see Section 3.3). On isotropic cases (Table 3), the mean value of the statistic $\hat{\delta}^\nu$ obtained for $\nu = 0$ increases as the value of h decreases, while, for $\nu = 2$, it remains constant around 0.8. This is due to the bias of the estimators $\hat{h}_1^\nu$ and $\hat{h}_2^\nu$. The standard deviation does not vary significantly according to h. However, we observe that they are slightly lower than the standard deviations of the previous statistics $\hat{\delta}^\nu$.

We set two rejection intervals for the second anisotropy test, by estimating the 0.95-quantile of the statistics $\hat{\delta}^\nu$ on isotropic data. We obtain $R^0 = \{|\hat{\delta}^0| > 0.32\}$ for $\nu = 0$ and $R^2 = \{|\hat{\delta}^2| > 0.2\}$ for $\nu = 2$. The evaluation of the test is reported in Tables 3 and 4. On isotropic fields (Table 3), the test defined for $\nu = 0$ failed detecting the isotropic fields with small Hurst index h whereas for $\nu = 2$, the second test has performances which are as good as the first test for all values of h.

On anisotropic fields (Table 4), results of the second test for $\nu = 0$ are worse than those of the first test for $\nu = 0$. This is due to the bias of the estimators $\hat{h}_1^\nu$ and $\hat{h}_2^\nu$ which produces errors in the evaluation of $\hat{\delta}^\nu$. For the second test, results obtained

			$\nu = 0$		$\nu = 2$	
$\lvert h_1 - h_2 \rvert$	h_1	h_2	$\hat{d}^0 \pm \sigma$	p	$\hat{d}^2 \pm \sigma$	p
0	0.9	0.9	0.04±0.03	100	0.08±0.07	99
0	0.7	0.7	0.±0.06	100	0.01±0.12	99
0	0.5	0.5	0.±0.07	97	0.01±0.14	95
0	0.3	0.3	0.05±0.04	98	0.12±0.09	93
0.2	0.9	0.7	0.18±0.05	32	0.2±0.06	79
0.3	0.9	0.5	0.35±0.06	0	0.38±0.1	22
0.6	0.9	0.3	0.45±0.06	0	0.52±0.14	6
0.2	0.7	0.5	0.17±0.06	43	0.19±0.13	84
0.4	0.7	0.3	0.35±0.05	0	0.43±0.13	21
0.2	0.5	0.3	0.17±0.07	41	0.22±0.13	74

TABLE 2. Estimation of the directional Hurst index differences obtained on fields simulated with spectral simulation techniques. The value p is the percentage of simulations classified into isotropic cases using the anisotropy test.

	$\nu = 0$		$\nu = 2$	
h	$\hat{\delta}^0 \pm \sigma$	p	$\hat{\delta}^2 \pm \sigma$	p
0.1	0.3±0.05	69	0.09±0.07	91
0.2	0.2±0.05	99	0.08±0.06	93
0.3	0.14±0.05	100	0.08±0.06	96
0.4	0.09±0.04	100	0.08±0.06	93
0.5	0.06±0.03	100	0.07±0.05	97
0.6	0.04±0.03	100	0.08±0.05	97
0.7	0.03±0.03	100	0.07±0.05	99
T	0.12±0.1	95	0.08±0.06	95

TABLE 3. Estimation of the directional Hurst index differences $h_1 - h_2$ on FBF simulated with Stein simulation technique. The estimators of $h_1 - h_2$ are $\hat{\delta}^\nu = |\max(\hat{h}_1^\nu, \hat{h}_2^\nu) - \min(\hat{h}_{01}, \hat{h}_{02})|$, for $\nu = 0, 2$. The value p is the percentage of simulations classified into isotropic using the anisotropy test on statistics $\hat{\delta}^\nu$.

with $\nu = 2$ are better than with $\nu = 0$. They are even equivalent to those of the first test with $\nu = 2$.

6. Application

6.1. **Material and methods.** Our database has a total of 58 cases, each case being composed of Full-Field Digital Mammograms (FFDM) of the left and right

			$\nu = 0$		$\nu = 2$	
$\lvert h_1 - h_2 \rvert$	h_1	h_2	$\hat{\delta}^0 \pm \sigma$	p	$\hat{\delta}^2 \pm \sigma$	p
0	0.9	0.9	0.07±0.03	100	0.05±0.04	100
0	0.7	0.7	0.04±0.04	100	0.07±0.05	96
0	0.5	0.5	0.04±0.03	100	0.01±0.08	89
0	0.3	0.3	0.07±0.03	100	0.18±0.08	56
0.2	0.9	0.7	0.18±0.03	100	0.13±0.07	78
0.3	0.9	0.5	0.33±0.04	42	0.27±0.07	17
0.6	0.9	0.3	0.42±0.03	0	0.34±0.09	17
0.2	0.7	0.5	0.15±0.05	100	0.1±0.07	86
0.4	0.7	0.3	0.3±0.03	73	0.23±0.09	36
0.2	0.5	0.3	0.12±0.04	100	0.07±0.06	93

TABLE 4. Estimation of the directional Hurst index differences obtained on fields simulated with spectral simulation techniques. The estimators of $h_1 - h_2$ are $\hat{\delta}^\nu = |\max(\hat{h}_1^\nu, \hat{h}_2^\nu) - \min(\hat{h}_{01}, \hat{h}_{02})|$, for $\nu = 0, 2$. The value p is the percentage of simulations classified into isotropic cases using the anisotropy test.

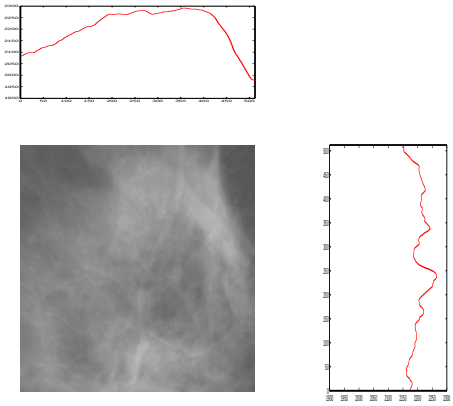

FIGURE 4. A ROI extracted from a FFDM and its vertical and horizontal projections (case id. 83, feb05, rm).

breasts of a woman. Images were acquired in MLO position using a Senographe 2000D (General Electric Medical Systems, Milwaukee, WI), with a spatial resolution of 0.1mm^2 per pixel (image size: 1914x2294 pixels). Images are courtesy of the Department of Radiology of the University of Pennsylvania. In each image of the database, we extracted manually a region of interest (ROI) of size 512×512 within the densest region of the breast. As illustrated on Figure 4, we then computed the discrete row- and column-wise projections of each ROI (Equation (18)) and

the estimates of the directional Hurst indices in both directions (Equation (20), for $\nu = 0, 2$). We also estimated the minimal Hurst index using the line-based estimators given in Equation (23). Note that in mammograms, vertical (row) and horizontal (column) directions (labeled 1 and 2) correspond to directions perpendicular and parallel to the chest wall, respectively.

6.2. **Mammogram regularity.** The estimates of the minimal Hurst index we obtained using line-based estimators on the extracted ROI are in the interval $[0.18; 0.42]$, with an average of 0.31 and a standard deviation of 0.05. On Figure 5 (a) and (b), we see that the line-based estimates of the minimal Hurst in both directions have equivalent empirical distributions and are approximately equal on each image. This observation is consistent with the theoretical result showing that line-based restrictions of AFBF have same Hurst indices in all directions (see Section 3.3). This gives an indirect evidence of the adequacy of the AFBF model to mammogram textures.

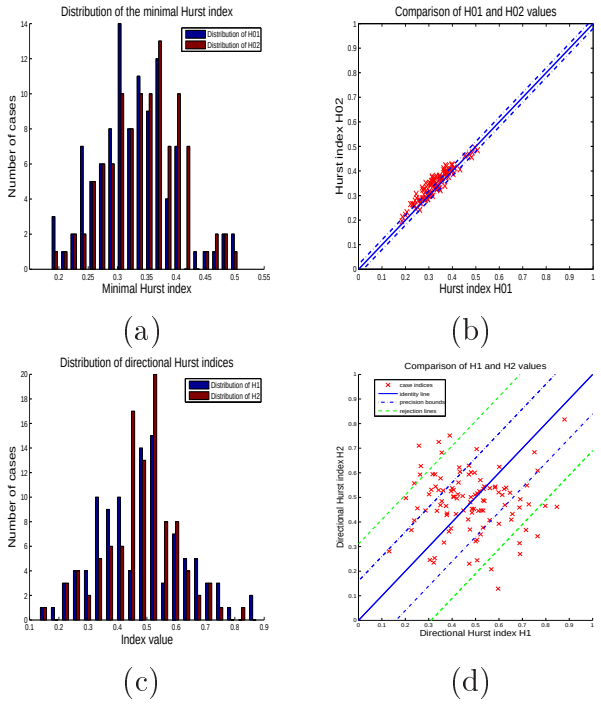

FIGURE 5. (a) Histograms of the minimal Hurst indices of mammograms, estimated using horizontal and vertical line-based estimators ($\hat{h}_{01}$ and $\hat{h}_{02}$). (b) Horizontal and vertical line-based estimates of the minimal Hurst index on all mammograms. (c) Histograms of the horizontal and vertical Hurst indices of mammograms estimated using horizontal and vertical projection-based estimators ($\hat{h}_1^2$ and $\hat{h}_2^2$). (d) Horizontal and vertical projection-based estimates of the minimal Hurst index on all mammograms.

6.3. **Mammogram anisotropy.** On Figure 5 (c), we observe that horizontal and vertical Hurst index estimates have similar distributions. Standard deviations of horizontal and vertical Hurst indices are about 0.15 and their averages are 0.45 and 0.55, respectively. On average, the mammograms seems slightly smoother in the direction parallel to the chest wall than in the perpendicular one. Besides, ranges of minimal and directional Hurst indices are not the same. This is partly due to differences in precision of index estimators. However, since the range difference is above the precision, this also indicates a texture anisotropy.

The mammogram anisotropy is further confirmed by results shown on Figures 6 (a), (b) and (c). On these figures, we plotted histograms of estimators which are used in the different anisotropy tests, and represented the rejection bounds of these tests by red dash lines. On Figure 6 (a), there is about 14 % of the mammograms for which the difference estimate $\hat{d}^2$ is above the rejection bound. In other words, the first anisotropy test defined for $\nu = 2$ detects very few anisotropic textures in the database. This is due to the lack of precision of the estimator $\hat{d}^\nu$ when the sampling factor $\nu = 2$. On Figure 6 (b), we see that the first anisotropy test for $\nu = 0$ detects more anisotropic textures than for $\nu = 2$: there is about 43 % of detected anisotropic cases. Recall however that anisotropic cases having different vertical and horizontal Hurst indices cannot be detected by the first test. Such cases are rather detected by the second test. Indeed, on Figure 6 (c), we observe that the second test (defined for $\nu = 2$) detects about 60 % of anisotropic cases. All of these results have to be interpreted carefully. They do not lead to the conclusion that in our database, there are 60 % of anisotropic cases and 40 % of isotropic cases. They only mean that there is at least 60 % of cases which, according to the AFBF model, can be considered as anisotropic with a confidence level of 95 %.

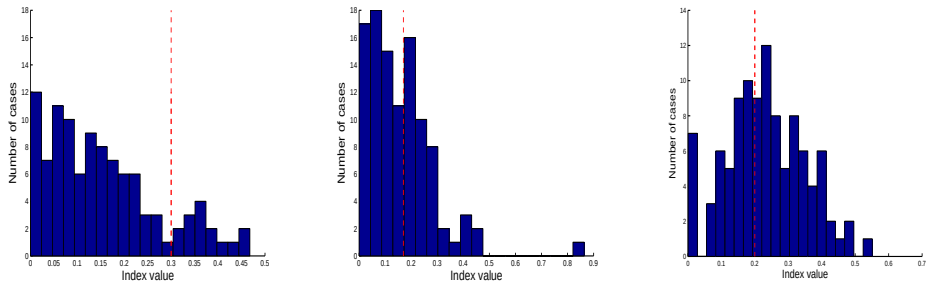

(a) (b) (c)

FIGURE 6. Histograms of estimators (a) $\hat{d}^2 = |\hat{h}_1^2 - \hat{h}_2^2|$, (b) $\hat{d}^0 = |\hat{h}_1^0 - \hat{h}_2^0|$, and (c) $\hat{\delta}^2 = |\max(\hat{h}_1^2, \hat{h}_2^2) - \min(\hat{h}_{01}, \hat{h}_{02})|$. The red dash lines represent the rejection bounds of isotropy tests corresponding to each estimator.

On Figure 7, we show some examples of extracted ROI, with their corresponding estimator values and test decisions. Notice that in some cases (e.g. image (a)),

the decision of the first test (with $\nu = 0$) is "anisotropy" whereas the one of the second test is "isotropy". This is due to the lack of precision of the estimator $\hat{\delta}^2$ of the second test. Also mention that in some cases (e.g. image (i)), the decision of the first test with $\nu = 2$ is "anisotropy" whereas it is "isotropy" with $\nu = 0$. Such decision difference can be an effect of the lack of accuracy of the estimator $\hat{d}^0$ of the first test.

7. Discussion and conclusion

The radiographic appearance of a breast mainly depends on the distribution and relative amount of adipose and fibroglandular tissues it contains. Whereas the adipose tissues are radiologically translucent and tend to produce dark images, the fibroglandular tissues attenuate X-ray and increase the image brightness. The density of a mammogram refers to the bright image aspect caused by the presence of fibroglandular tissues in the breast. At the end of the 60's, Wolfe put forth the idea that the breast cancer risk could be assessed from the observation of mammogram appearance and patterns [56, 55]. This pioneer work gave rise to an important medical debate. Later on, some investigators started focusing on the relationship between the breast density and the breast cancer risk [15, 16]. They provided first evidences that an increased breast density is associated to an increased cancer risk. These evidences were further confirmed by many subsequent epidemiological studies (see [34, 35] for an exhaustive review). These studies have shown the medical importance of the mammogram density.

In many epidemiological studies, the evaluation of the density is done qualitatively by radiologists and is thus subject to inter-observer variability. Hence, early in the 90's, some investigators attempted to define quantitative and automated measurements of the density using mathematical tools; see the numerous references in the proceedings of the International Workshops on Digital Mammography [4, 30, 32, 41, 49, 58]. In particular, some of these investigators used the fractal dimension as an indicator of the mammogram density [19, 20, 21]. More recently, some authors studied more deeply the stochastic nature of the mammogram density by using FBF-related stochastic models such as 1/f noise models [18, 33, 36, 43]. As in the work presented here, these authors put many efforts into the measurement of model parameters on mammograms and the empirical validation of models.

Measurements of Hurst-related parameters on FFDM and film mammograms have been reported independently in several papers [18, 19, 21, 33, 36, 43]. Caldwell et al. [21] and Byng et al. [19, 20] used the Box counting technique to estimate the fractal dimension on the whole image. They reported estimations obtained on 70 film mammograms. Values are between 2.2 and 2.5 (with an estimated precision of 0.02), which corresponds to a minimal Hurst index between 0.46 and 0.77. Kestener et al. computed the Hurst index on small regions of size 512×512 of film mammograms taken from the DDSM database [43]. The values of the minimal Hurst index are in $[0.20; 0.35]$ and $[0.55; 0.75]$ for ROI with predominant adipose and dense tissues,

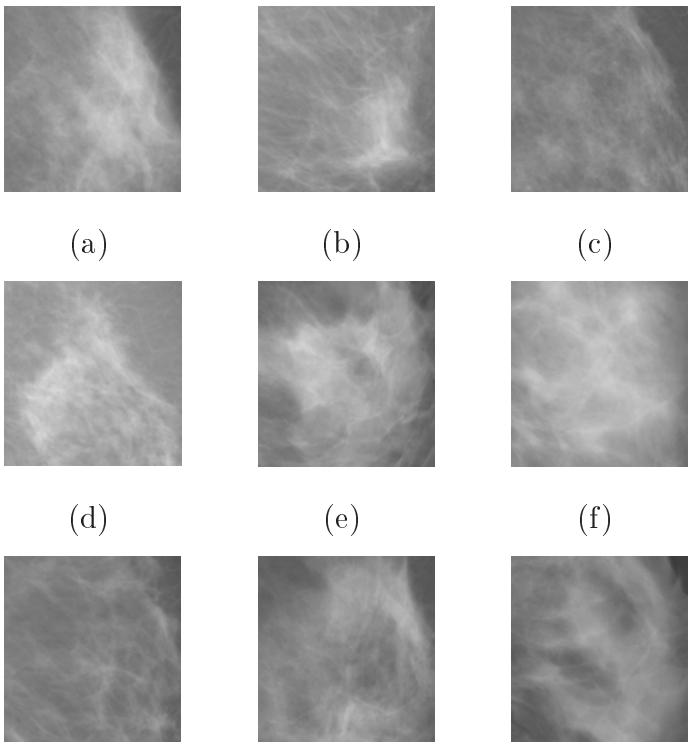

(a) (b) (c)

(d) (e) (f)

(g) (h) (i)

image	case id.	$\hat{h}_{min}$	$\hat{h}_1^2$	$\hat{h}_2^2$	$\lvert\hat{d}^2\rvert$	IR	$\lvert\hat{d}^0\rvert$	IR	$\lvert\hat{\delta}^2\rvert$	IR
(a)	95, jun03, lm	0.32	0.33	0.25	0.07	I	**0.19**	**A**	**0.01**	**I**
(b)	76, oct03, lm	0.36	0.38	0.43	0.05	I	0.05	I	0.07	I
(c)	74, dec04, lm	0.39	0.50	0.32	0.18	I	0.01	I	0.11	I
(d)	86, mar05, lm	0.33	0.35	0.44	0.05	I	0.28	A	0.11	I
(e)	83, feb05, lm	0.37	0.52	0.45	0.08	I	0.17	A	0.15	I
(f)	85, mar05, lm	0.26	0.48	0.45	0.03	I	0.15	A	0.22	I
(g)	73, dec04, lm	0.35	0.72	0.55	0.17	I	0.22	A	0.37	A
(h)	83, feb05, rm	0.32	0.73	0.47	**0.26**	**A**	**0.01**	**I**	0.41	A
(i)	85, mar05, rm	0.26	0.39	0.75	0.36	A	0.14	I	0.49	A

FIGURE 7. Some ROI extracted from FFDM with their estimated indices. Columns IR give decisions of the anisotropy tests based on the estimators $|\hat{d}^0|$, $|\hat{d}^2|$ and $|\hat{\delta}^2|$ (A=anisotropic, I=isotropic).

respectively. In [36], authors used a spectral method for the estimation of the regularity coefficient β of the 1/f noise model. On 104 ROI extracted from 26 FFDM mammograms, $\beta \in [1.32; 1.44]$, which correspond to $H \in [0.33; 0.42]$. In another study, same authors reported values $\beta = [1.42, 1.51]$, i.e. $H = [0.42; 0.51]$ on extracted ROI of 60 film mammograms [33]. These values are in accordance with

those obtained independently in [18]. The values we obtained using the line-based estimators are close to those obtained by Heine et al. [36] on FFDM mammograms: they are slightly lower due probably to (a) the estimation technique difference and (b) to the selection of the ROI which in our study can be of low density.

Similarly to [18, 33, 36], our experiments confirm the relevance of fractional Brownian models for the characterization of the mammogram density. However, they also reveal that the isotropy assumption which is behind the mammogram modeling of [18, 33, 36] is not valid in many cases: around 60 percents of the mammogram textures we studied could be considered as anisotropic with a high level of confidence. Hence, we conclude that AFBF model is more realistic and relevant than the isotropic FBF model for the description of FFDM textures.

From a medical point of view, this conclusion suggests taking into account the anisotropy for the analysis of the mammogram density and the evaluation of a breast cancer risk. However, the establishment of a relationship between the anisotropy and the breast cancer risk is beyond the scope of this paper. The conclusion of this paper can be seen as an encouraging starting point for future medical investigations. Up to now, we have shown that the AFBF model enables to extract some significant density features which are not captured by the usual FBF. We have also constructed a mathematical methodology for analysing those features. In collaboration with radiologists, we plan to further evaluate the medical relevance of the density anisotropy for the assessment of the breast cancer risk.

The interest of this paper is not restricted to results concerning the mammogram application. The methodology we proposed for characterizing and testing the anisotropy of Brownian textures is generic. We believe that this methodology could be useful in many medical applications, such as the analysis of osteoporosis from bone radiographs. The methodology includes some original statistical tests of anisotropy, based on estimates of directional Hurst indices. We showed a new theoretical result about the estimator convergence, which gives a mathematical foundation to the construction of those tests. The statistical tests were also validated on simulated data. The discussion which comes with experiments gives some helpful information on how to correctly use and interpret the anisotropy tests in practice.

Appendix A. Proof of Theorem 3.1

Proof. The key point of the proof relies on the introduction of an auxiliary estimator. Let us denote $Z^\nu_{1,u}$, respectively $Z^\nu_{2,u}$, the second-order increments of $Y_1(t) = \int_{\mathbb{R}} X(s,t)\rho(s)ds$, respectively $Y_2(t) = \int_{\mathbb{R}} X(t,s)\rho(s)ds$, as defined by (11). We consider estimators defined from generalized quadratic variations $V^\nu_{1,u}$ and $V^\nu_{2,u}$ of $Z^\nu_{1,u}$ and $Z^\nu_{2,u}$, according to (12), by

$$T^\nu_{1,u} = V^\nu_{1,u}/\mathbb{E}\left(V^\nu_{1,u}\right) \text{ and } T^\nu_{2,u} = V^\nu_{2,u}/\mathbb{E}\left(V^\nu_{2,u}\right).$$

Without loss of generality we can also assume that $h_1 \leq h_2$. Usual computations on generalized quadratic variations lead to

$$T^{\nu}_{e,u} \underset{2^{-\nu}M\to+\infty}{\longrightarrow} 1 \text{ a. s. with } \sqrt{2^{-\nu}M}\left(T^{\nu}_{e,u}-1\right) \underset{2^{-\nu}M\to+\infty}{\longrightarrow} \mathcal{N}(0,\sigma^{u}_{e,u}),$$

for $e,u \in \{1,2\}$, where for $v \in \{1,2\}$

$$\sigma^{v}_{e,u} = C^{v}_{u}\left(h_e+\frac{1}{2}\right)/(uv)^{2h_e+1}E\left(h_e+\frac{1}{2}\right)^2, \tag{29}$$

with $C^{v}_{u}(H) = 4\sum_{p\in\mathbb{Z}}\left(\int_{\mathbb{R}} e^{-ip\xi}(1-e^{-iu\xi})^2(1-e^{iv\xi})^2|\xi|^{-2H-1}d\xi\right)^2$ and $E(H) = \int_{\mathbb{R}}\left|(e^{-i\xi}-1)^2\right|^2|\xi|^{-2H-1}d\xi$, which are finite positive constants for $H<2$ (see Theorem 2.3 of [13] for instance). It is straightforward to see that the vector $\left(T^{\nu}_{e,u}\right)_{1\leq e,u\leq 2}$ converges to $(1)_{1\leq e,u\leq 2}$ almost surely as $2^{-\nu}M\to+\infty$. Let us prove the asymptotic normality. Let us remark that for any $(a_{e,u})_{1\leq e,u\leq 2}$ positive numbers one can write

$$\sum_{1\leq e,u\leq 2} a_{e,u}\left(T^{\nu}_{e,u}-1\right) = \frac{1}{\mathbb{E}\left(V^{\nu}_{1,1}\right)}\sum_{1\leq e,u\leq 2} a_{e,u}\frac{\mathbb{E}\left(V^{\nu}_{1,1}\right)}{\mathbb{E}\left(V^{\nu}_{e,u}\right)}\left(V^{\nu}_{e,u}-\mathbb{E}\left(V^{\nu}_{e,u}\right)\right).$$

From Proposition 1. 1 of [13] we get

$$a_{e,u}\frac{\mathbb{E}\left(V^{\nu}_{1,1}\right)}{\mathbb{E}\left(V^{\nu}_{e,u}\right)} = b_{e,u}(2^{-\nu}M)^{-2(h_1-h_e)}\left(1+\underset{2^{-\nu}M\to+\infty}{O}(2^{\nu}M^{-1})\right),$$

with $b_{e,u} = a_{e,u}\frac{E\left(h_1+\frac{1}{2}\right)}{E\left(h_e+\frac{1}{2}\right)}u^{-2h_e-1}$. Let us write

$$\sum_{1\leq e,u\leq 2} b_{e,u}(2^{-\nu}M)^{-2(h_1-h_e)}\left(V^{\nu}_{e,u}-\mathbb{E}\left(V^{\nu}_{e,u}\right)\right) \overset{d}{=} \sum_{k=1}^{n}\lambda_{k,M}\left(\varepsilon^2_{k,M}-1\right),$$

where $n = 2^{-\nu+2}M-8$, $(\varepsilon_{k,M})_{1\leq k\leq n}$ is a sequence of independent standard Gaussian variables and $(\lambda_{k,M})_{1\leq k\leq n}$ are the eigenvalues of the covariance matrix of

$$\left\{\frac{Z^{\nu}_{e,u}(p)}{\sqrt{2^{-\nu}M-2u+1}}; 1\leq e,u\leq 2,\ 0\leq p\leq 2^{-\nu}M-2u\right\}.$$

Let $s^2_n = \mathrm{Var}\left(\sum_{1\leq e,u\leq 2} b_{e,u}(2^{-\nu}M)^{-2(h_1-h_e)}\left(V^{\nu}_{e,u}-\mathbb{E}\left(V^{\nu}_{e,u}\right)\right)\right)$. Following a Lindeberg condition [26] we obtain that

$$s^{-1}_n\sum_{1\leq e,u\leq 2} b_{e,u}(2^{-\nu}M)^{-2(h_1-h_e)}\left(V^{\nu}_{e,u}-\mathbb{E}\left(V^{\nu}_{e,u}\right)\right) \underset{2^{-\nu}M\to+\infty}{\longrightarrow} \mathcal{N}(0,1), \tag{30}$$

as soon as $\max_k |\lambda_{k,n}| = \underset{2^{-\nu}M\to+\infty}{o}(s_n)$. On the one hand, an upper bound for $\max_k |\lambda_{k,n}|$ is given by

$$C2^{\nu}M^{-1}\max_{1\le e,u\le 2}\max_{0\le p\le 2^{-\nu}M-2u}\sum_{1\le e',u'\le 2}\sum_{p'=0}^{2^{-\nu}M-2u'}\left|\mathrm{Cov}\left(Z^{\nu}_{e,u}(p),(2^{-\nu}M)^{-2(h_1-h_{e'})}Z^{\nu}_{e',u'}(p')\right)\right|.$$

According to Proposition 1.2 of [13], one can find $C_\nu > 0$ such that

$$\sum_{p'=0}^{2^{-\nu}M-2u'}\left|\mathrm{Cov}\left(Z^{\nu}_{e,u}(p),(2^{-\nu}M)^{-2(h_1-h_e)}Z^{\nu}_{e,u'}(p')\right)\right| \le C(2^{-\nu}M)^{-2h_1-1}\log(2^{-\nu}M),$$

for any $0 \le p \le 2^{-\nu}M - 2u$. It remains to consider the covariance terms between $Z^{\nu}_{1,u}$ and $Z^{\nu}_{2,u'}$. Using the spectral representation of the random field X we get

$$\mathrm{Cov}\left(Z^{\nu}_{1,u}(p),Z^{\nu}_{2,u'}(p')\right) = \int_{\mathbb{R}^2} e^{i\frac{2^{\nu}p\xi_2}{M}}e^{-i\frac{2^{\nu}p'\xi_1}{M}}(1-e^{iu\frac{2^{\nu}\xi_2}{M}})^2(1-e^{-iu'\frac{2^{\nu}\xi_1}{M}})^2 f(\xi)\widehat{\rho}(\xi_1)\overline{\widehat{\rho}(\xi_2)}d\xi,$$

where $\widehat{\rho}(\xi_e) = \int_{\mathbb{R}} e^{is\xi_e}\rho(s)ds$ is the Fourier transform of the window function. Therefore

$$\left|\mathrm{Cov}\left(Z^{\nu}_{1,u}(p),Z^{\nu}_{2,u'}(p')\right)\right| \le C(2^{-\nu}M)^{-4},$$

with

$$C = (uu')^2\int_{\mathbb{R}^2}\xi_2^2\xi_1^2 f(\xi)\widehat{\rho}(\xi_1)\overline{\widehat{\rho}(\xi_2)}d\xi < +\infty.$$

Then $\max_k |\lambda_{k,n}| = \underset{2^{-\nu}M\to+\infty}{O}((2^{-\nu}M)^{-2h_1-2}\log(2^{-\nu}M))$. On the other hand, since $(a_{e,u})_{1\le e,u\le 2}$ are positive numbers, using the fact that

$$\mathrm{Cov}\left(Z^{\nu}_{e,u}(p)^2,(2^{-\nu}M)^{-2(h_1-h_{e'})}Z^{\nu}_{e',u'}(p')^2\right) = 2\mathrm{Cov}\left(Z^{\nu}_{e,u}(p),(2^{-\nu}M)^{-2(h_1-h_{e'})}Z^{\nu}_{e',u'}(p')\right)^2 \ge 0,$$

we get

$$s_n^2 \ge \sum_{1\le e,u\le 2} b_{e,u}^2(2^{-\nu}M)^{-4(h_1-h_e)}\mathrm{Var}\left(V^{\nu}_{e,u}\right) \ge c(2^{-\nu}M)^{-4h_1-3},$$

from Proposition 1.2 of [13], for some $c > 0$. Then (30) holds. Let us remark that $\frac{s_n}{\mathbb{E}(V^{\nu}_{1,1})} = \sqrt{2^{-\nu}M}\left(\sqrt{a\Gamma a^t} + \underset{2^{-\nu}M\to+\infty}{O}(2^{\nu}M^{-1})\right)$ with $a = \begin{pmatrix} a_{1,1} & a_{1,2} & a_{2,1} & a_{2,2}\end{pmatrix}$ and

$$\Gamma = \begin{pmatrix} \sigma^1_{1,1} & \sigma^2_{1,1} & 0 & 0\\ \sigma^2_{1,1} & \sigma^2_{1,2} & 0 & 0\\ 0 & 0 & \sigma^1_{2,1} & \sigma^2_{2,1}\\ 0 & 0 & \sigma^2_{2,1} & \sigma^2_{2,2}\end{pmatrix}.$$

We therefore get an asymptotic normality for $\sum_{1\le e,u\le 2} a_{e,u}\left(T^{\nu}_{e,u}-1\right)$, for any $(a_{e,u})_{1\le e,u\le 2}$ positive numbers. Using tightness criterion and uniqueness of the limit law we can claim that $\sqrt{2^{-\nu}M}\left(T^{\nu}_{e,u}-1\right)_{1\le e,u\le 2} \underset{2^{-\nu}M\to+\infty}{\longrightarrow} \mathcal{N}(0,\Gamma)$.

By Taylor Formula for the function $g(x_{1,1},x_{1,2},x_{2,1},x_{2,2}) = \log\left(\frac{x_{1,2}}{x_{1,1}}\right) - \log\left(\frac{x_{2,2}}{x_{2,1}}\right)$ (see Theorem 3.3.11 in [27] for instance) we get that almost surely $\log\left(\frac{T^\nu_{1,2}}{T^\nu_{1,1}}\right) - \log\left(\frac{T^\nu_{2,2}}{T^\nu_{2,1}}\right) \underset{2^{-\nu}M\to+\infty}{\longrightarrow} 0$ with $\sqrt{2^{-\nu}M}\left(\log\left(\frac{T^\nu_{1,2}}{T^\nu_{1,1}}\right) - \log\left(\frac{T^\nu_{2,2}}{T^\nu_{2,1}}\right)\right) \underset{2^{-\nu}M\to+\infty}{\overset{d}{\longrightarrow}} \mathcal{N}(0, a\Gamma a^t)$ for $a = \nabla g(1,1,1,1) = (\ -1 \quad 1 \quad 1 \quad -1\ )$.
From (14), $2\log(2)\left(\hat{H}^\nu_1 - \hat{H}^\nu_2\right)$ is equal to

$$\log\left(\frac{\mathbb{E}\left(V^\nu_{1,2}\right)}{\mathbb{E}\left(V^\nu_{1,1}\right)}\right) - \log\left(\frac{\mathbb{E}\left(V^\nu_{2,2}\right)}{\mathbb{E}\left(V^\nu_{2,1}\right)}\right) + \log\left(\frac{\mathbb{E}\left(T^\nu_{1,2}\right)}{\mathbb{E}\left(T^\nu_{1,1}\right)}\right) - \log\left(\frac{\mathbb{E}\left(T^\nu_{2,2}\right)}{\mathbb{E}\left(T^\nu_{2,1}\right)}\right),$$

with for $e \in \{1,2\}$, by Proposition 1.1 of [13],

$$\frac{\mathbb{E}\left(V^\nu_{e,2}\right)}{\mathbb{E}\left(V^\nu_{e,1}\right)} = 2^{2h_e+1}\left(1 + \underset{2^{-\nu}M\to+\infty}{o}\left(1/\sqrt{2^{-\nu}M}\right)\right).$$

Then,

$$\hat{H}^\nu_1 - \hat{H}^\nu_2 = h_1 - h_2 + \frac{1}{2\log(2)}\left(\log\left(\frac{\mathbb{E}\left(T^\nu_{1,2}\right)}{\mathbb{E}\left(T^\nu_{1,1}\right)}\right) - \log\left(\frac{\mathbb{E}\left(T^\nu_{2,2}\right)}{\mathbb{E}\left(T^\nu_{2,1}\right)}\right)\right) + \underset{2^{-\nu}M\to+\infty}{o}\left(1/\sqrt{2^{-\nu}M}\right),$$

such that, with $\gamma = \frac{a\Gamma a^t}{4\log(2)^2}$,

$$\hat{H}^\nu_1 - \hat{H}^\nu_2 \underset{2^{-\nu}M\to+\infty}{\longrightarrow} h_1 - h_2 \text{ a.s., with } \sqrt{2^{-\nu}M}\left(\hat{H}^\nu_1 - \hat{H}^\nu_2 - (h_1 - h_2)\right) \underset{2^{-\nu}M\to+\infty}{\overset{d}{\longrightarrow}} \mathcal{N}(0,\gamma)$$

□

Acknowledgments. Authors are grateful to Dr. Bakic and Dr. Maidment (University of Pennsylvania) for offering them the opportunity to study FFDM mammograms acquired in their department of Radiology. This work was supported by the grant ANR-NT05-142030 of the "Agence National pour la Recherche".

References

[1] P. Abry, P. Gonçalves, and F. Sellan. Wavelet spectrum analysis and 1/f processes. In *Lecture Notes in Statistics*, volume 103, pages 15–30. Springer-Verlag, 1995.

[2] P. Abry and F. Sellan. The wavelet-based synthesis for fractional Brownian motion proposed by F. Sellan and Y. Meyer: remarks and fast implementation. *Appl. Comput. Harmon. Anal.*, 3:377–383, 1996.

[3] R. J. Adler. *The Geometry of Random Field*. John Wiley & Sons, 1981.

[4] S. Astley et al., editors. *8th International Workshop on Digital Mammography*, LNCS, 4046, Manchester, UK, June 2004. Springer.

[5] A. Ayache, A. Bonami, and A. Estrade. Identification and series decomposition of anisotropic Gaussian fields. *Proceedings of the Catania ISAAC05 congress*, 2005.

[6] J. M. Bardet, G. Lang, G. Oppenheim, et al. Generators of long-range dependence processes: a survey. In *Theory and applications of long-range dependence*, pages 579–623. Birkhauser Boston, 2003.

[7] J. M. Bardet, G. Lang, G. Oppenheim, et al. Semi-parametric estimation of the long-range dependence parameter: a survey. In *Theory and applications of long-range dependence*, pages 557–577. Birkhauser Boston, 2003.
[8] A. Benassi, S. Jaffard, and D. Roux. Elliptic Gaussian random processes. *Rev. Mathem. Iberoamericana*, 13(1):19–89, 1997.
[9] C.L. Benhamou, S. Poupon, E. Lespessailles, et al. Fractal analysis of radiographic trabecular bone texture and bone mineral density. *Journal of Bone and Mineral Research*, 16(4):697–703, 2001.
[10] D. Benson, M. M. Meerschaert, B. Bäumer, and H. P. Scheffler. Aquifer operator-scaling and the effect on solute mixing and dispersion. *Water Resour. Res.*, 42:1–18, 2006.
[11] J. Beran. *Statitics for long-memory processes*. Chapman Hall London, 1994.
[12] H. Biermé, M. M. Meerschaert, and H. P. Scheffler. Operator scaling stable random fields. *Stoch. Proc. Appl.*, 117(3):312–332, 2007.
[13] H. Biermé and F. Richard. Estimation of anisotropic gaussian fields through radon transform. *ESAIM: Probability and Statistics*, 2007.
[14] A. Bonami and A. Estrade. Anisotropic analysis of some Gaussian models. *J. Fourier Anal. Appl.*, 9:215–236, 2003.
[15] N.F. Boyd, B. O'Sullivan, J.E. Campbell, et al. Mammographic signs as risk factors for breast cancer. *Br. J. Cancer*, 45:185–193, 1982.
[16] J. Brisson, F. Merletti, NL Sadowsky, et al. Mammographic features of the breast and breast cancer risk. *Am J. Epidemiol.*, 115(3):428–437, 1982.
[17] B. Brunet-Imbault, G. Lemineur, C. Chappard, et al. A new anisotropy index on trabecular bone radiographic images using the fast Fourier transform. *BMC Med. Imaging*, 5(4), 2005.
[18] A. Burgess, F. Jacobson, and P. Judy. Human observer detection experiments with mammograms and power-law noise. *Med. Phys.*, 28(4):419–437, 2001.
[19] J. Byng, N. N. Boyd, and E. others Fishell. Automated analysis of mammographic densities. *Phys. Med. Biol.*, 41:909–923, 1996.
[20] J. Byng, M. Yaffe, G. Lockwood, et al. Automated analysis of mammographic densities and breast carcinoma risk. *Cancer*, 80(1):66–74, 1997.
[21] C. Caldwell, S. Stapleton, D. Holdsworth, et al. Characterisation of mammographic parenchymal patterns by fractal dimension. *Phys. Med. Biol.*, 35(2):235–247, 1990.
[22] G. Chan. An effective method for simulating Gaussian random fields. In *Proceedings of the statistical Computing section*, pages 133–138. Amerir. Statist., 1999.
[23] C.-C. Chen, J. Daponte, and M. Fox. Fractal feature analysis and classification in medical imaging. *IEEE Trans. on Med. Imaging*, 8(2):133–142, 1989.
[24] J. F. Coeurjolly. *Inférence statistique pour les mouvements browniens fractionnaires et multifractionnaires*. PhD thesis, University Joseph Fourier, 2000.
[25] G. Cross and A. Jain. Markov random field texture models. *IEEE Trans PAMI*, 5(1):25–39, 1983.
[26] M. CzÃ¶rgo and P. RÃ©vÃ©sz. *Strong approximation in probability and statistics*. Academic Press, 1981.
[27] D. Dacunha-Castelle and M. Duflo. *ProbabilitÃ©s et statistiques*, volume 2. Masson, 1983.
[28] S. Davies and P. Hall. Fractal analysis of surface roughness by using spatial data. *J. R. Stat. Soc. Ser. B*, 61:3–37, 1999.
[29] C. R. Dietrich and G. N. Newsam. Fast and exact simulation of stationary gaussian processes through circulant embedding of the covariance matrix. *SIAM J. Sci. Comput.*, 18(4):1088–1107, 1997.
[30] K. Doi et al., editors. *3rd International Workshop on Digital Mammography*, Chicago, USA, June 1996. Elsevier Science.

[31] K. J. Falconer. *Fractal Geometry*. John Wiley & Sons, 1990.
[32] A.G. Gale et al., editors. *2nd International Workshop on Digital Mammography*, York, England, July 1994. Elsevier Science.
[33] J. Heine, S. Deine, R. Velthuizen, et al. On the statistical nature of mammograms. *Med. Phys.*, 26(11):2254–2269, 1999.
[34] J. Heine and P. Malhorta. Mammographic tissue, breast cancer risk, serial image analysis, and digital mammography: serial breast tissue change and related temporal influences. *Acad. Radiol*, 9:317–335, 2002.
[35] J. Heine and P. Malhorta. Mammographic tissue, breast cancer risk, serial image analysis, and digital mammography: tissue and related risk factors. *Acad. Radiol*, 9:298–316, 2002.
[36] J. Heine and R. Velthuizen. Spectral analysis of full field digital mammography data. *Med. Phys.*, 29(5):647–661, 2002.
[37] J. Istas and G. Lang. Quadratic variations and estimation of the local Holder index of a Gaussian process. *Ann. Inst. Henri Poincaré, Prob. Stat.*, 33(4):407–436, 1997.
[38] R. Jennane, R. Harba, G. Lemineur, et al. Estimation of the 3D self-similarity parameter of trabecular bone from its projection. *Medical Image Analysis*, 11:91–98, 2007.
[39] A. Kamont. On the fractional anisotropicwiener field. *Probab. Math. Statist.*, 16:85–98, 1996.
[40] L. M. Kaplan and C. C. J. Kuo. An Improved Method for 2-d Self-Similar Image Synthesis. *IEEE Trans. Image Process.*, 5(5):754–761, 1996.
[41] N. Karssemeijer et al., editors. *4th International Workshop on Digital Mammography*, Nijmegen, The Netherlands, June 1998. Kluwer Academic.
[42] J. T. Kent and A. T. A. Wood. Estimating the fractal dimension of a locally self-similar Gaussian process by using increments. *J. Roy. Statist. Soc. Ser. B*, 59(3):679–699, 1997.
[43] P. Kestener, J.-M. Lina, P. Saint-Jean, et al. Wavelet-based multifractal formalism to assist in diagnosis in digitized mammograms. *Image Anal. Stereol.*, 20:169–174, 2001.
[44] S. Leger. *Analyse stochastique de signaux multi-fractaux et estimations de paramètres.* PhD thesis, Université d'Orléans, `http://www.univ-orleans.fr/SCIENCES/MAPMO/publications/leger`, 2000.
[45] T. Lundahl, W.J. Ohley, S.M. Kay, and R. Siffe. Fractional brownian motion: a maximum likelihood estimator and its application to image texture. *IEEE Trans. on Medical Images*, 5(3):152–161, 1986.
[46] B. B. Mandelbrot and J. Van Ness. Fractional Brownian motion, fractionnal noises and applications. *SIAM Review*, 10:422–437, 1968.
[47] Y. Meyer, F. Sellan, and M.S. Taqqu. Wavelets, Generalised White Noise and Fractional Integration: The Synthesis of Fractional Brownian Motion. *J. Fourier Anal. Appl.*, 5(5):465–494, 1999.
[48] I. Norros and P. Mannersalo. Simulation of Fractional Brownian Motion with Conditionalized Random Midpoint Displacement. Technical report, Advances in Performance analysis, 1999.
[49] H.-O. Peitgen, editor. *6th International Workshop on Digital Mammography*, Bremen, Germany, June 2002. Springer.
[50] R.F. Peltier and J. Levy Vehel. Multifractional Brownian motion: definition and preliminary results. Technical report, INRIA, 1996.
[51] A. Pentland. Fractal-based description of natural scenes. *IEEE Trans. on Patt. Anal. and Mach. Intell.*, 6:661–674, 1984.
[52] E. Perrin, R. Harba, R. Jennane, and I. Iribarren. Fast and Exact Synthesis for 1-D Fractional Brownian Motion and Fractional Gaussian Noises. *IEEE Signal Processing Letters*, 9(11):382–384, 2002.
[53] V. Pipiras. Wavelet-based simulation of fractional Brownian motion revisited. Preprint, 2004.

[54] M. L. Stein. Fast and exact simulation of fractional Brownian surfaces. *J. Comput. Graph. Statist.*, 11(3):587–599, 2002.
[55] J.N. Wolfe. Ducts as a sole indicator of breast carcinoma. *Radiology*, 89:206–210, 1967.
[56] J.N. Wolfe. A study of breast parenchyma by mammography in the normal woman and those with benign and malignant disease. *Radiology*, 89:201–205, 1967.
[57] Y. Xiao. Sample path properties of anisotropic gaussian random fields. *preprint*, 2007.
[58] M. Yaffe et al., editors. *5th International Workshop on Digital Mammography*, Toronto, Canada, June 2000. Medical Physics Publishing.

Laboratory MAP5, University Paris Descartes, CNRS UMR 8145, 45, rue des Saints-Pères, 75270 PARIS cedex 06 FRANCE.
E-mail address: [richard,bierme]@math-info.univ-paris5.fr